Available online at www.sciencedirect.com
ScienceDirect
Catalysis Today 126 (2007) 203–210
CATALYSIS TODAY
www.elsevier.com/locate/cattod

# *In situ* synchrotron small-angle X-ray scattering study of MCM-41 crystallisation using Gemini surfactants

E. Gianotti [a], G. Berlier [a,*], K. Costabello [a], S. Coluccia [a], F. Meneau [b,1]

[a] *Dipartimento di Chimica IFM and NIS, Centre of Excellence, University of Turin, v. P. Giuria 7, 10125 Torino, Italy*
[b] *Netherlands Organisation for Scientific Research (NWO), DUBBLE/CRG ESRF BP220, F38043 Grenoble Cedex, France*

Available online 18 September 2006

**Abstract**

The synthesis of ordered mesoporous MCM-41, performed at room temperature with Gemini surfactants as structure directing agents, was followed by *in situ* time-resolved small-angle X-ray scattering with synchrotron radiation source. This study evidenced that the mesostructure evolution can be described considering two main steps. In the initial stage, upon addition of the silica source to the Gemini solution, small aggregates are formed as indicated by broad and weak features in the X-ray scattering patterns. By performing a Guinier analysis and determining the pair size distribution functions $p(r)$, the presence of cylindrical particles of 20 Å in radius and 40 Å length is evidenced. These particles are non-interacting isolated silicate-encrusted micelles, that are the precursors of the mesostructured silica growth. In the second stage, Bragg diffraction peaks appear, indicating that the cylindrical precursors are joining together to form a structure with higher degree of organization. Initially, only small crystalline domains are visible, which then merge to a long range ordered 2D hexagonal structure. X-ray scattered data allows to follow the gradual polymerisation of silica on the surface of cylindrical micelles, giving the final product in less then 10 min. The evolution of crystallinity fraction with time was used to get information about the kinetics and the growth mechanism involved.


*Keywords:* Gemini surfactants; Small-angle X-ray scattering; Mesoporous MCM-41

## 1. Introduction

The discovery of ordered mesoporous silica materials (M41S family) [1], with pore size tuneable from 25 to 100 Å, has attracted great interest for their applications as heterogeneous catalysts [2], optical and conducting materials [3], and as host–guest systems [4,5]. Research activity was mainly focused on the optimisation of the synthesis procedure, to obtain materials with uniform pore size and high thermal stability, and on the understanding of the mechanisms of the silica crystallisation, as recently reviewed by Patarin et al. [6]. MCM-41 is one of the most common 2D hexagonal mesoporous materials; a ''true'' liquid crystal template mechanism, where silica polymerises around a preformed organized micellar phase, was firstly proposed for its crystallisation [1]. This hypothesis was mainly based on the observation that the structure and morphology of MCM-41 were similar to surfactants/water liquid crystals, nevertheless could not explain why the mesostructure could be formed at surfactant concentrations below the critical concentration necessary to the liquid crystal formation [7].

A more general reaction pathway for the crystallisation of ordered mesoporous silicas considers the cooperative formation of inorganic/organic interfaces, which is mainly based on the strong Coulombic interaction between the cationic head groups of the surfactant and anionic silicate species [8]. Depending upon the synthesis conditions, a lamellar to hexagonal phase transition was observed during the synthesis of MCM-41, which was explained in terms of optimisation of the charge density matching at the interface along the crystallisation [8]. As recently pointed out, the interaction between the inorganic precursor and the organic template is the key factor in the control of the mesostructure formation, but the specific synthesis mechanism strictly depends upon the reaction conditions (such as type and concentration of surfactant, pH, silica source, etc.) [6].

* Corresponding author. Tel.: +39 0116707856; fax: +39 0116707953.
*E-mail address:* gloria.berlier@unito.it (G. Berlier).
[1] Present address : Synchrotron Soleil, L'Orme des Merisiers, Saint-Aubin, BP48, 91192 Gif sur Yvette Cedex, France.

0920-5861/$ – see front matter © 2006 Published by Elsevier B.V.
doi:10.1016/j.cattod.2006.08.064

Anionic, cationic and non-ionic surfactants have been exploited as structure directing agent (SDA) to produce different structural phases of ordered mesoporous materials [9]. Mesoporous MCM-41 is traditionally synthesized by hydrothermal synthesis using alkyltrimethylammonium halide surfactants (e.g. cetyltrimethylammonium bromide). An alternative class of surfactants, Gemini, can be used as SDA to obtain mesoporous systems with highly controlled structure and enhanced thermal stability. To synthesize MCM-41 materials, cationic Gemini surfactants, having two ammonium groups, each with a hexadecyl hydrophobic chain linked by a polymethylene spacer of variable length ($C_{16\text{-}n\text{-}16}$ $2Br^-$), can be used [10–13]. These cationic Gemini allow to perform the synthesis at room temperature without hydrothermal conditions.

By changing the length of the polimethylene spacer, it is possible to direct the synthesis to one of the M41S phases; using a Gemini with spacer varying from 4 to 10 C atoms ($C_{16\text{-}4\text{-}16}$/$C_{16\text{-}10\text{-}16}$), hexagonal MCM-41 phase is synthesized, while with a $C_{16\text{-}12\text{-}16}$ and $C_{16\text{-}3\text{-}16}$ Gemini, MCM-48 and MCM-50 phases are, respectively, obtained. The length of the C-spacer also affects the structural parameters, such as thickness of the silica walls, pores and channel sizes. This versatility can be explained by the influence of the spacer length on the head group area, which influences the charge density matching at the organic/inorganic interface [11].

In the present paper, time-resolved small-angle X-ray scattering (SAXS) is applied to follow the complete crystallisation process of MCM-41. Many research groups have shown that SAXS can be successfully employed to follow the crystallisation of ordered micro and mesoporous structures [14–19]. SAXS is a non-destructive method, does not require special sample preparation and permits the *in situ* reaction analysis. The SAXS patterns at low angles bear information about nanoscale inhomogeneities (shape and size of small particles or clusters), whereas the Bragg peaks at higher angles reflect the internal ordering in the system. The evolution of the micellar phase during the silica crystallisation was followed to understand the mechanism of the MCM-41 mesostructure arrangement when Gemini surfactants are employed as SDA.

## 2. Experimental

($C_{16\text{-}4\text{-}16}$) Gemini surfactants were synthesized by the reaction of alkanediyl-α,ω-bis(dimethylamine) with alkyl bromide [20].

The MCM-41 synthesis [11] was performed at room temperature, by quickly inserting the reaction solution in a specially conceived cell that allowed to follow *in situ* the crystallisation process. The cell was composed by two copper slabs separated by a Teflon thickness, equipped with mica windows (for further details see http://www.esrf.fr/UsersAndScience/Experiments/CRG/BM26/SaxsWaxs/Sxwxsample/Temperature).

A Gemini aqueous solution was prepared under stirring at 40 °C, and subsequently added with NaOH to obtain pH 12. Immediately before starting the *in situ* SAXS experiment, silica source tetraethylorthosilicate (TEOS) was added, the solution was quickly mixed and inserted in the measurement apparatus. The obtained mixed solution was then measured in static conditions. The final molar composition of the gel mixture was $C_{16\text{-}n\text{-}16}$:0.06/NaOH:0.65/$H_2O$:150/TEOS:1, corresponding to a Gemini concentration of 22 mmol.

SAXS measurements were performed at station BM26b, DUBBLE CRG beamline of the ESRF, Grenoble, France with an X-ray photon energy of 12 keV. The time resolution of 10 s/frame was used. A photon counting position sensitive area detector was used. Experiments were carried out with a sample-detector distance of 1.5 m, which corresponds to scattering vector ranges $q$, of 0.026–0.475 $Å^{-1}$. The scattering vector ($q$-axis) was calibrated with the scattering pattern of silver behenate, a silver salt of a long chain carboxylic acid ($AgC_{22}H_{43}O_2$). The required amount of reacting solution was inserted into the cell and the scans were started at time $t_0$, which was typically approximately 3 min after loading the solutions. The solution measured before TEOS addition (Gemini + NaOH) was subtracted as background. The data reduction and analysis of the time-resolved SAXS was processed using BSL and XOTOKO softwares, provided by Central Laboratory of the Research Councils (CCLRC, http://www.cclrc.ac.uk) via Collaborative Computational Project 13 (CCP13).

## 3. Results and discussion

In the present paper, small-angle X-ray scattering is employed to study the structure of self-organized mesoporous MCM-41 using Gemini as SDA. To fully exploit the information content in the SAXS data, comprehensive analysis of the scattering profiles is performed yielding a consistent model of the structural organization of crystallites.

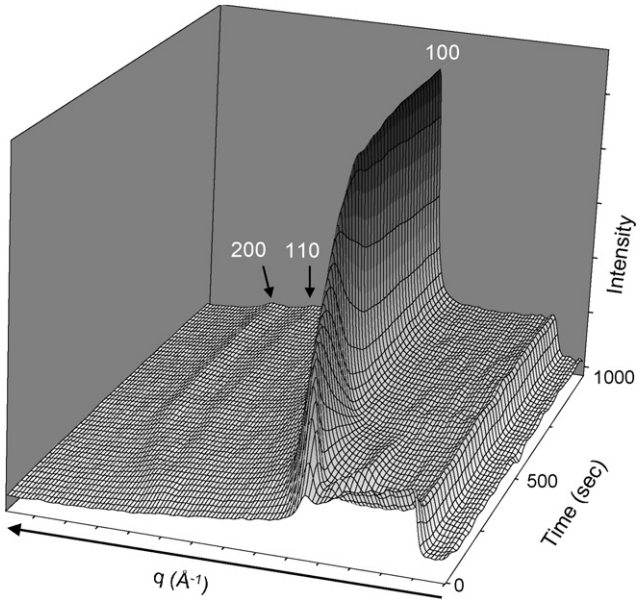


Fig. 1. Stacked 3D small-angle X-ray scattering profile of the MCM-41 synthesis in the $q$ range 0.026–0.475 $Å^{-1}$, from $t_0$ to $t_0$ + 1000 s (time resolution 10 s/frame).

Stacked 3D small-angle X-ray scattering profiles measured *in situ* during the formation of the 2D hexagonal MCM-41 as a function of reaction time are shown in Fig. 1. Measurements were started after the addition of TEOS to the required amount of reacting solution (Gemini + NaOH), that was inserted in the measurement cell. The scans were started at time $t_0$, which was typically 3 min after loading the solutions. The spectrum of the solution before TEOS addition was used as reference for the background subtracted spectra reported in Fig. 1 (spectra obtained by radial integration of the 2D detector).

By a detailed analysis of the SAXS data reported in Fig. 1 (*vide infra*), two main steps can be outlined: in the first stage ($t_0$ + 20 s) only broad features are observed, and in the second one Bragg diffraction peaks are formed. These two steps can be appreciated in Fig. 2 where the 2D detector images (and corresponding spectra obtained by radial integration) measured at the beginning ($t_0$ + 10 s) and at the end ($t_0$ + 1000 s) of the reaction are reported.

Together with the two main steps described above, a weak signal is observable in the low $q$ region ($q < 0.1$ Å$^{-1}$) in the first 5 min of the reaction. This weak signal gradually shifts to lower $q$ values with time. After around $t_0$ + 300 s, this feature fades away, masked by the low $q$ tail of the main Bragg diffraction peak.

The structure determination of the synthesis intermediates, associated with the two synthesis steps, will be addressed in the following sections using detailed analysis.

### 3.1. First step: X-ray scattering analysis

In the first two frames ($t_0$ + 20 s) measured after TEOS addition to the Gemini solution, only a broad hump at $q = 0.12$ Å$^{-1}$ is observed. This feature is due to the precursors formation, a consequence of the Coulombic interactions at the inorganic/organic interface, that evolves with time towards a more ordered 2D material.

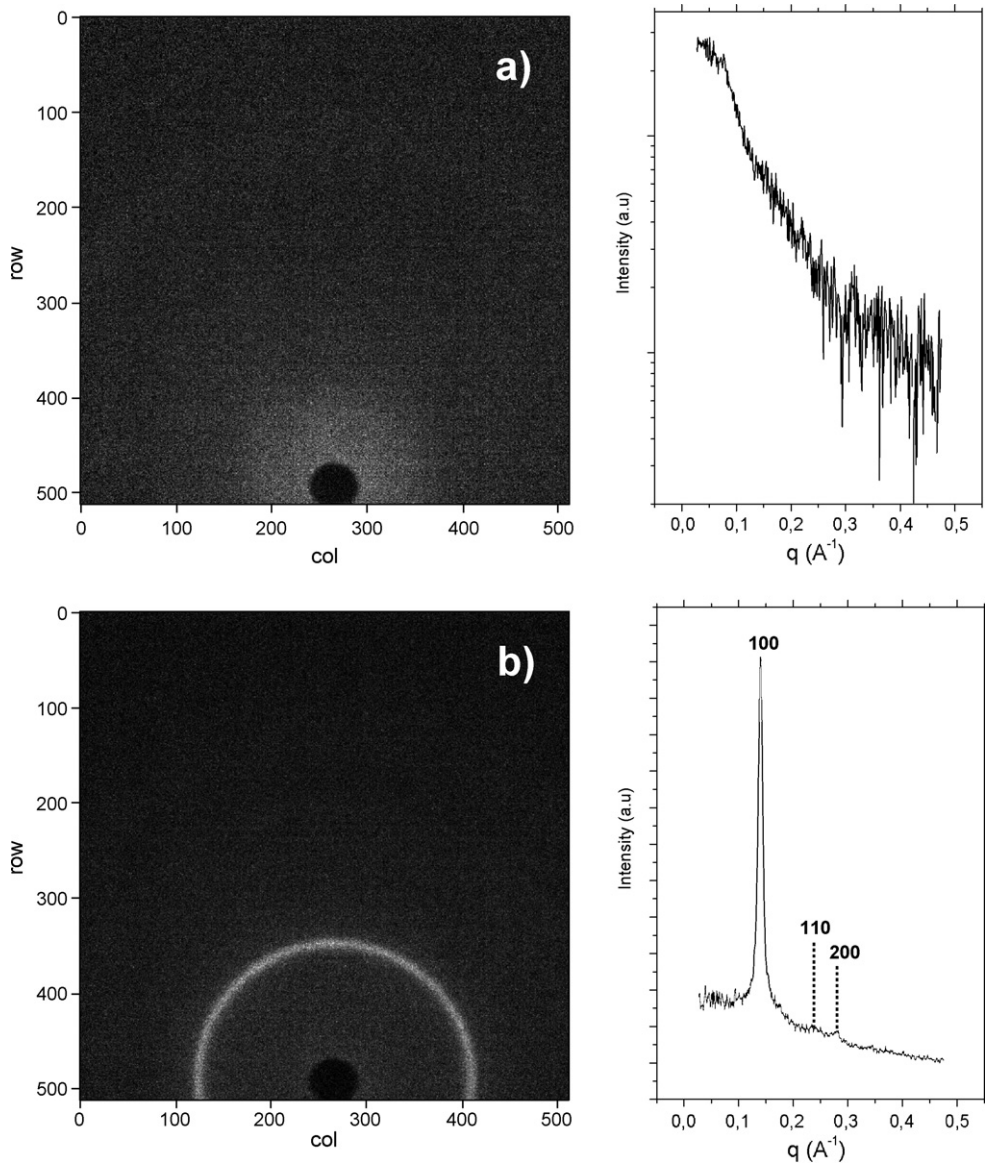


Fig. 2. 2D X-ray scattering images (left) and corresponding spectra obtained by radial integration (right) measured after (a) $t_0$ + 10 s and (b) $t_0$ + 1000 s.

The distance distribution functions $p(r)$ are determined in order to obtain information about the size and shape of the involved precursors. Moreover, analysis of the small-angle X-ray scattering in the Porod region is also performed for a more complete identification of such intermediates.

### 3.1.1. Particles size and the Guinier region

In the low $q$ region or Guinier region, the SAXS intensity can be approximated by:

$$I(q) = C \exp\left(\frac{-R_g^2 q^2}{3}\right) \quad (1)$$

where $C$ is a scaling constant, $q$ the scattering vector and $R_g$ is the Guinier radius or radius of gyration.

The experimental SAXS data, where no diffraction has occurred, were fitted using the GNOM software [21], enabling us to determine the Guinier radius. For the first two frames of the reaction, the value of the radius of gyration $R_g$ deduced from the fits is equal to $17 \pm 1$ Å. The Guinier value is useful for determining the particle sizes only if information about the shape is available. This latter information can be obtained by using the distance distribution functions, $p(r)$.

The scattering data were thus transformed into pair distance distribution functions (PDDF) using the indirect Fourier transform GNOM software [21] according to the following equation:

$$p(r) = (2\pi^2)^{-1} \int_0^{D_{max}} I(q) q(r) \sin(qr)\, dq \quad (2)$$

where $D_{max}$ is the maximum diameter of the particle and $q$ is the scattering vector. The PDDF (Fig. 3) of the initial stages of the reaction ($t_0 + 20$ s), displays a tail toward high values of $r$, suggesting that elongated/cylindrical particles are formed, of radius $R = 20$ Å and length $L = 40$ Å. This is in agreement with the Guinier radius obtained above, which is related to the radius $R$ and length $L$ of the cylinders by the following geometric relation: $R_g{}^2 = (R^2/2) + (L^2/12)$

These values are compatible with the presence of micellar agglomerates, covered by a silica phase. Similar results, concerning the formation of non-interacting isolated cylindrical particles, were observed as precursors in the formation of ordered mesoporous structures prepared by using different SDA, indicating a similar growth mechanism [18,22].

### 3.1.2. Fractal analysis

Fig. 4 shows a clearer view of the scattering profile changes of the first two frames (log $I(q)$ versus log $q$), before the onset of crystallisation. Unlike the report on zeolite $A$ synthesis by Sankar et al., no marked features associated with the presence of clear primary units are visible in the SAXS scattering profile [15,19].

The intensity $I(q)$ closely follows a power-law decay $q^{-n}$ (where $n \sim 2$) which is slower than the asymptotic behaviour of $I(q)$ with $n \sim 4$ predicted by the Porod law for compact particles with sharp interfaces. This indicates that this system is more complex. Very similar decay of the scattering intensity has already been observed in various SAXS studies conducted on the crystallisation of different types of microporous/mesoporous materials [23].

By focusing on the $q$-range between 0.025 and 0.13 Å$^{-1}$ and after removing the leading $q^{-2}$ decay, the plots $I(q) \times q^2$ versus log $q$ (Fig. 5) exhibit a broad maximum ($q_{max} = 0.105$ Å$^{-1}$) which can be fitted with a Gaussian function. The inverse of the calculated $q_{max}$ provides the size of the aggregates/precursors leading to MCM-41 crystallites. The corresponding reciprocal value of $2\pi/q_{max}$ approximates to ca. 62 Å. This value is in agreement with the size of cylindrical particles calculated with PDDF.

## 3.2. Second step: Bragg diffraction pattern

In the second step of the reaction, the small cylindrical aggregates, described above, evolve toward an higher spatial organization, as evidenced by the appearance of a Bragg peak ($q = 0.11$ Å$^{-1}$) at $t_0 + 30$ s. At the end of the reaction ($t_0 + 1000$ s), the SAXS pattern shows three rings, which after radial integration, yield three Bragg peaks on the SAXS intensity curve (Fig. 2b). At $t_0 + 1000$ s the intense peak at $q = 0.14$ Å$^{-1}$ is indexed to the (1 0 0) plane, and the two weak

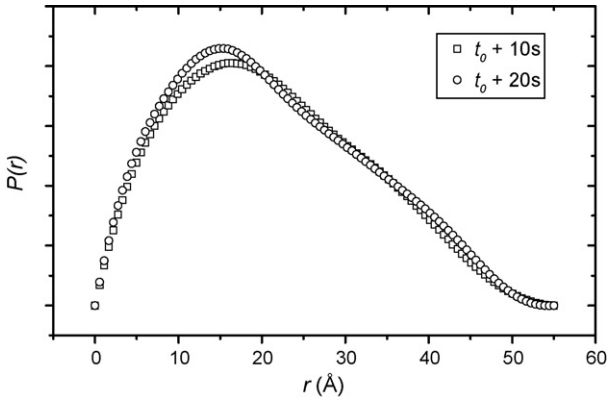


Fig. 3. Pair size distribution functions $p(r)$ of the first two frames of the synthesis reaction. Frame 1: open squares; frame 2: open circles.

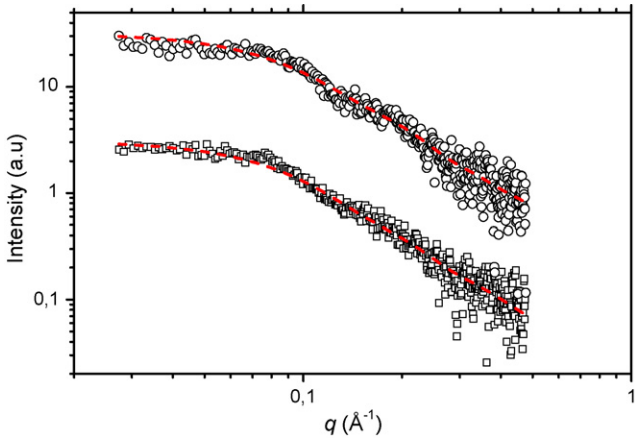


Fig. 4. Log $I(q)$ vs. log $q$ scattering profiles of the first two frames. Frame 1: open squares; frame 2: open circles.

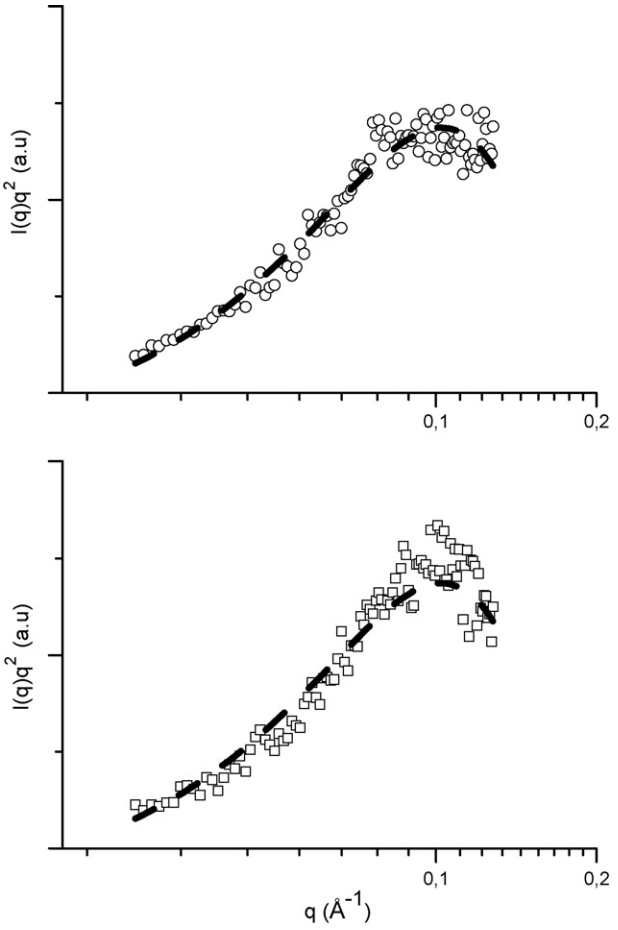


Fig. 5. Plot of $I(q) \times q^2$ vs. log $q$ after removing the leading $q^{-2}$ decay, with the Gaussian fit. Frame 1: open squares; frame 2: open circles.

peaks at $q = 0.24$ and 0.28 Å$^{-1}$ to the (1 1 0) and (2 0 0) planes, respectively. This diffraction pattern indicates a homogeneous pore size and regular wall thickness of the mesoporous material. The peaks have been indexed in the two-dimension hexagonal system *P6mm*, with a *d*-spacing of 45 Å. From this value, the unit cell size $a_o = 2d_{10}/\sqrt{3} = 52$ Å was calculated. These values are in good agreement with the structural parameters measured *ex situ* on MCM-41 samples synthesized by using Gemini as SDA (results available as Supplementary Material).

As a general remark, we underline that the peaks intensity is low due to the presence of the surfactant micelles within the MCM-41 pores, that leads to a substantial loss of scattering contrast between channels and walls.

Coming to the evolution of the Bragg pattern with time, distinct phenomena can be underlined. First, the peak indexed to the (1 0 0) plane gradually increases in intensity while the reaction proceeds. At the same time, the peak shifts to higher $q$ values (from 0.11 at $t_0$ + 10 s to 0.14 Å$^{-1}$ at $t_0$ + 1000 s). After a short period from the growth of the (1 0 0) peak, the two minor features indexed to the (1 1 0) and (2 0 0) planes start to be visible. Due to the low resolution of these two peaks, the precise moment of their appearance cannot be easily appreciated. The evolution with time of the (1 0 0) peak

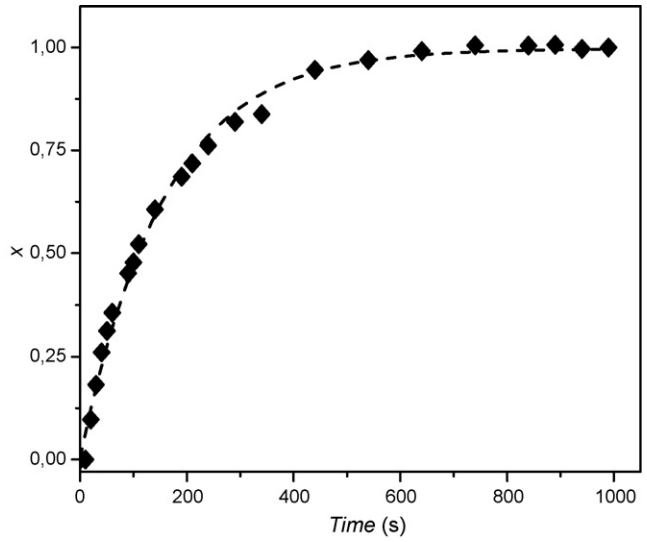


Fig. 6. Fraction of MCM-41 crystallisation as a function of time, obtained from the increasing area of the peak related to the (1 0 0) reflection of *P6mm* structure.

can be used to get information about the growth of the mesostructure.

In particular, the increasing area of the (1 0 0) peak was used to calculate the fraction of MCM-41 crystallisation, that is reported in Fig. 6 as a function of time. The intensity was determined by fitting the (1 0 0) Bragg peaks with a Gaussian function and measuring the corresponding areas. These areas were converted to the extent of reaction ($\alpha$), scaled from 0 to 1, using the relationship

$$\alpha(t) = \frac{I_{hkl}(t)}{I_{hkl}(\max)} \tag{3}$$

where $I_{hkl}(t)$ is the area of a given peak at time $t$ and $I_{hkl}$(max) is the maximum area of this peak. Fig. 6 clearly shows that the crystallisation gradually proceeds with time, reaching a plateau after 450 s, where the final ordered product is formed.

The evolution of diffraction peak intensity as a function of time can be used to derive more detailed information on the kinetics and the mechanism involved in the crystallisation process. Kinetic data and information both on the dimensionality and the crystallisation process are derived from the Avrami–Erofe'ev expression that is widely used to model phase transitions and crystal growth in solid-state chemistry using the extent of the reaction, $\alpha$, to time $t$ in the relationship [24–27]:

$$\alpha = 1 - \exp\left[-(k(t - t_0))^n\right] \tag{4}$$

where $t_0$ is the induction time, $k$ the rate constant, and $n$ is the Avrami exponent. The exponent $n$, ranging from $n = 0.5$ to $n = 4$, can be used in most cases to deduce information about the rate of nucleation and the mechanism of nuclei growth. This method has been applied successfully to model various solid-state reactions [28,29]. A Sharp–Hancock plot (ln $[-\ln(1-\alpha)]$ versus ln(time)), shown in Fig. 7, is used to determine the gradient $n$ and intercept $n$ ln k, and displays its linearity over the whole reaction. The deduced values of $n$ and $k$ are, respectively,

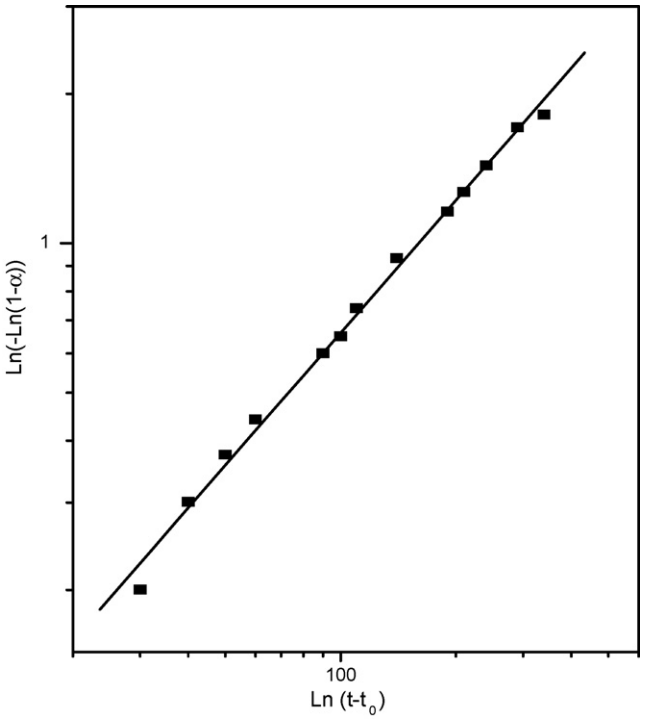


Fig. 7. Sharp–Hancock plot for the formation of MCM-41 over the range $0.15 < \alpha < 0.8$.

0.89 and $6 \times 10^{-3}$ $s^{-1}$. These values suggest that the MCM-41 crystallisation follows a one-dimensional growth, similarly to that recently reported for the crystallisation of AlPO-5 and CoAPO-5 [29].

Concerning the shift of the (1 0 0) peak to higher $q$ values during the crystallisation process, a plateau is reached after 450 s, when the crystallisation fraction reaches its maximum. This can be appreciated in Fig. 8 where the evolution with time of the $d_{1\,0\,0}$-spacing, obtained by $d_{1\,0\,0} = 2\pi/q$, is reported together with the full-width at half maximum (FWHM) of the same reflection. Fig. 8 shows that during the reaction, the $d_{1\,0\,0}$ value decreases from 58 to 45 Å, this final value being in agreement with the structural parameters of MCM-41 prepared by Gemini synthesis (*vide infra*). Since $d_{1\,0\,0}$-spacing in hexagonal mesoporous materials is related to the wall thickness, the observed trend is consistent with a progressive condensation of the inorganic walls by silica polymerisation [1,8,9,22].

In Fig. 8, the $d_{1\,0\,0}$ FWHM dependence upon time is also reported. The peak width reaches a maximum at around 200 s and then decreases reaching a plateau at around 450 s. At this time, the complete crystallisation process has occurred as evidenced when the fraction of crystallisation (Fig. 6) and the evolution of $d_{1\,0\,0}$-spacing with time (Fig. 8) are considered. The trend of FWHM with reaction time can be explained by assuming the development of small crystalline domains, formed by the merging of the small cylindrical particles observed in the first moments of the reaction. At this stage of the reaction ($t < t_0 + 200$ s) the small domains are not characterized by long range order, so that only the (1 0 0) Bragg peak can be appreciated. Gradually, these small domains join together, forming an ordered 2D mesostructure with long range order, as testified by the growth of the (1 1 0) and (2 0 0) Bragg peaks. The decrease of $q_{100}$ FWHM for $t > t_0 + 200$ s (see Fig. 8) is in agreement with the increase of the crystalline fraction, that is of the long range order of the mesostructure.

### 3.3. X-ray scattering intensity at low q values

The evolution with time of the X-ray scattered intensity at low $q$ values can be better appreciated in Fig. 9, where a different view of the stacked 3D data measured in the first 5 min of reaction is reported. The weak signal at $q < 0.1$ $Å^{-1}$ indicated by a arrow in Fig. 9, is formed around $t_0 + 40$ s and gradually moves to lower $q$ with time. After $t_0 + 200$ s this feature is no more observable in the spectra, probably due to the

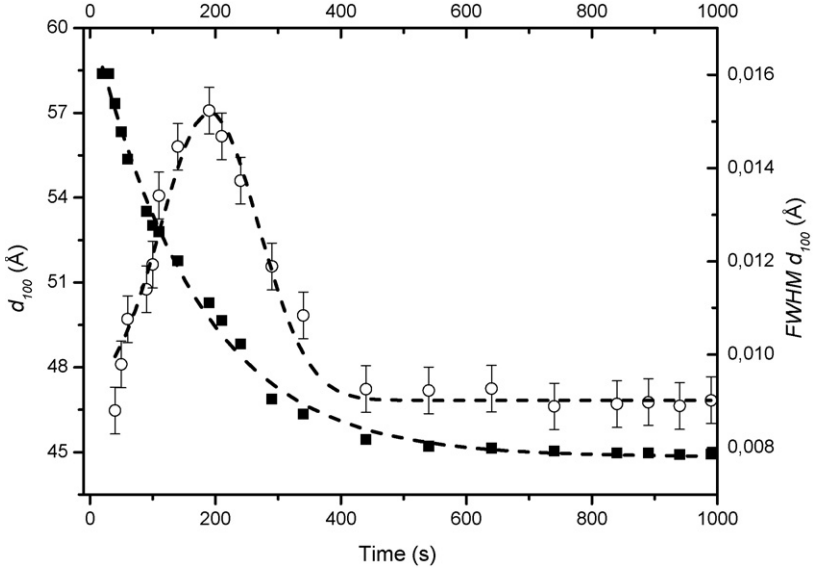


Fig. 8. The evolution with time of $d$-spacing (■) and FWHM (○) of (1 0 0) reflection of the hexagonal mesophase.

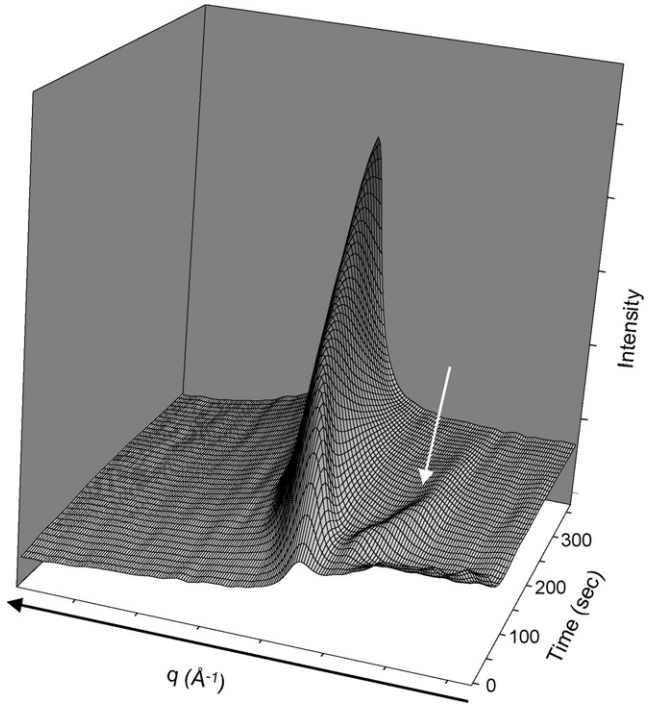


Fig. 9. A different view ($q$ range 0.050–0.162 Å$^{-1}$, from $t_0$ to $t_0$ + 300 s Å$^{-1}$, time resolution 10 s/frame) of the stacked 3D X-ray scattering profile reported in Fig. 1 allowing to appreciate the evolution with time of the intensity in the low $q$ region (indicated by an arrow).

strong overlapping of the low frequency tail of (1 1 0) peak. The corresponding $d$-spacing, calculated as $2\pi/q_{max}$ varies from 66 to 78 Å, that is higher values with respect to the ones calculated for the first two frames of reaction (see above, Section 3.1).

As anticipated above, a detailed analysis of the small-angle scattering intensity at $q < 0.1$ Å$^{-1}$ is complicated by the presence of the (1 0 0) peak and of the beamstop. An attempt to reconstruct *ab initio* the low resolution structure, from the initial portions of the scattering patterns was made using the program DAMMIN [30], but no sensible results were obtained. This feature could be interpreted in terms of a form factor, related to precursors of the mesostructure formation. However, the signal is related to particles bigger than the cylindrical ones evolving to form a Bragg diffraction pattern. Moreover, the evolution with time of this intensity does not seem to be correlated with the two steps described above. As a consequence, we suggest that the signal at $q < 0.1$ Å$^{-1}$ is related to the formation of an extra-phase, probably amorphous, not directly connected to the main crystallisation process of ordered MCM-41. This hypothesis will be verified by new experiments.

## 4. Conclusions

Highly ordered mesoporous MCM-41 was obtained by room temperature synthesis using $C_{16\text{-}4\text{-}16}$ Gemini surfactants as SDA. Time-resolved *in situ* small-angle X-ray scattering studies allow to follow the precursors formation and crystallisation process. In the first stage of the reaction, immediately after the silica source addition to the Gemini solution, non-ordered small aggregates can be detected. The size and shape of such particles were calculated by performing a Guinier analysis and determining the pair size distribution functions $p(r)$, giving cylindrical shape with size of 20 Å in radius and 40 Å length. These features, compatible with the presence of non-interacting isolated silicate-encrusted micelles, indicate that a cooperative self-assembly mechanism occurs.

In the second stage, the cylindrical particles join together, to gradually form a structure with higher degree of organization. Initially, small ordered domains are formed, which then merge together, producing a long range order mesostructure. The Bragg diffraction pattern present at the end of the reaction ($t_0$ + 1000 s) is typical of a 2D hexagonal system *P6mm*, with a $d$-spacing of 45 Å. The gradual shift to higher $q$ of the main Bragg peak (1 0 0) during the crystallisation indicates that the ordered 2D structure gradually condenses, as a consequence of silica polymerisation on the surface of micelles. Information on the kinetics and the involved growth mechanism has been obtained by using the Avrami–Erofe'ev expression, that implies a nucleation and growth mechanism. This analysis allowed the determination of a rate constant $k = 6 \times 10^{-3}$ s$^{-1}$, and of the parameter $n = 0.89$, which implies one-dimensional growth.

## Acknowledgments

Dr. P.L. Quagliotto is acknowledged for the help in the Gemini surfactants synthesis and for fruitful discussion. G.B. thanks the financial support from national FISR project. The Netherlands Organisation for Scientific Research (NWO) is acknowledged for granting us beamtime at DUBBLE/ESRF.

## Appendix A. Supplementary data

Supplementary data associated with this article can be found, in the online version, at doi:10.1016/j.cattod.2006.08.064.

## References

[1] J.S. Beck, J.C. Vartuli, W.J. Roth, M.E. Leonowicz, C.T. Kresge, K.D. Schmitt, C.T.W. Chu, D.H. Olson, E.W. Sheppard, S.B. McCullen, J.B. Higgins, J.L. Schlenker, J. Am. Chem. Soc. 114 (1992) 10834.
[2] A. Corma, Chem. Rev. 97 (1997) 2373.
[3] F. Marlow, M.D. McGehee, D.Y. Zhao, B.F. Chmelka, G.D. Stucky, Adv. Mater. 11 (1999) 632.
[4] D. Bruhwiler, G. Calzaferri, Microporous Mesoporous Mater. 72 (2004) 1.
[5] M. Hartmann, Chem. Mater. 17 (2005) 4577.
[6] J. Patarin, B. Lebeau, R. Zana, Curr. Opin. Colloid Interface Sci. 7 (2002) 107.
[7] J. Frasch, B. Lebeau, M. Soulard, J. Patarin, R. Zana, Langmuir 16 (2000) 9049.
[8] A. Monnier, F. Schüth, Q. Huo, D. Kumar, D. Margolese, R.S. Maxwell, G.D. Stucky, M. Krishnamurty, P. Petroff, A. Firouzi, M. Janicke, B.F. Chmelka, Science 261 (1993) 1299.
[9] J.M. Thomas, Angew. Chem. Int. Ed. 38 (1999) 3588.
[10] Q.S. Huo, D.I. Margolese, G.D. Stucky, Chem. Mater. 8 (1996) 1147.
[11] Q.S. Huo, D.I. Margolese, U. Ciesla, P.Y. Feng, T.E. Gier, P. Sieger, R. Leon, P.M. Petroff, F. Schüth, G.D. Stucky, Nature 368 (1994) 317.
[12] Q.S. Huo, R. Leon, P.M. Petroff, G.D. Stucky, Science 268 (1995) 1324.

[13] F.J. Romero, C. Jimenez, I. Huc, R. Oda, Microporous Mesoporous Mater. 69 (2004) 43.
[14] P. de Moor, T.P.M. Beelen, B.U. Komanschek, L.W. Beck, P. Wagner, M.E. Davis, R.A. van Santen, Chem. Eur. J. 5 (1999) 2083.
[15] P. de Moor, T.P.M. Beelen, R.A. van Santen, L.W. Beck, M.E. Davis, J. Phys. Chem. B 104 (2000) 7600.
[16] K. Flodström, C.V. Teixeira, H. Amenitsch, V. Alfredsson, M. Lindén, Langmuir 20 (2004) 4885.
[17] V. Alfredsson, H. Amenitsch, K. Flodström, M. Lindén, C.V. Teixeira, H. Wennerstrom, Nanoporous Mater. Iv 156 (2005) 69.
[18] A.Y. Khodakov, V.L. Zholobenko, M. Imperor-Clerc, D. Durand, J. Phys. Chem. B 109 (2005) 22780.
[19] W. Fan, M. O'Brien, M. Ogura, M. Sanchez-Sanchez, C. Martin, F. Meneau, K. Kurumada, G. Sankar, T. Okubo, PCCP Phys. Chem. Chem. Phys. 8 (2006) 1335.
[20] R. Zana, M. Benrraou, R. Rueff, Langmuir 7 (1991) 1072.
[21] D.I. Svergun, J. Appl. Crystallogr. 25 (1992) 495.
[22] M. Lindén, S.A. Schunk, F. Schüth, Angew. Chem. Int. Ed. 37 (1998) 821.
[23] P. de Moor, T.P.M. Beelen, B.U. Komanschek, O. Diat, R.A. van Santen, J. Phys. Chem. B 101 (1997) 11077.
[24] M. Avrami, J. Chem. Phys. 7 (1939) 1103.
[25] M. Avrami, J. Chem. Phys. 8 (1940) 212.
[26] M. Avrami, J. Chem. Phys. 9 (1941) 177.
[27] B.C.R. Erofe'ev, Dokl. Acad. Sci. URSS 52 (1946) 511.
[28] A.M. Fogg, S.J. Price, R.J. Francis, S. O'Brien, D. O'Hare, J. Mater. Chem. 10 (2000) 2355.
[29] D. Grandjean, A.M. Beale, A.V. Petukhov, B.M. Weckhuysen, J. Am. Chem. Soc. 127 (2005) 14454.
[30] D.I. Svergun, Biophys. J. 76 (1999) 2879.